LETTER

doi:10.1038/nature14499

Bipolar seesaw control on last interglacial sea level

G. Marino[1], E. J. Rohling[1,2], L. Rodríguez-Sanz[1], K. M. Grant[1], D. Heslop[1], A. P. Roberts[1], J. D. Stanford[3] & J. Yu[1]

Our current understanding of ocean–atmosphere–cryosphere interactions at ice-age terminations relies largely on assessments of the most recent (last) glacial–interglacial transition[1–3], Termination I (T-I). But the extent to which T-I is representative of previous terminations remains unclear. Testing the consistency of termination processes requires comparison of time series of critical climate parameters with detailed absolute and relative age control. However, such age control has been lacking for even the penultimate glacial termination (T-II), which culminated in a sea-level highstand during the last interglacial period that was several metres above present[4]. Here we show that Heinrich Stadial 11 (HS11), a prominent North Atlantic cold episode[5,6], occurred between 135 ± 1 and 130 ± 2 thousand years ago and was linked with rapid sea-level rise during T-II. Our conclusions are based on new and existing[6–9] data for T-II and the last interglacial that we collate onto a single, radiometrically constrained chronology. The HS11 cold episode[5,6] punctuated T-II and coincided directly with a major deglacial meltwater pulse, which predominantly entered the North Atlantic Ocean and accounted for about 70 per cent of the glacial–interglacial sea-level rise[8,9]. We conclude that, possibly in response to stronger insolation and CO_2 forcing earlier in T-II, the relationship between climate and ice-volume changes differed fundamentally from that of T-I. In T-I, the major sea-level rise clearly post-dates[3,10,11] Heinrich Stadial 1. We also find that HS11 coincided with sustained Antarctic warming, probably through a bipolar seesaw temperature response[12], and propose that this heat gain at high southern latitudes promoted Antarctic ice-sheet melting that fuelled the last interglacial sea-level peak.

Late Quaternary glacial–interglacial cycles exemplify the response of Earth's climate to combined insolation and CO_2 forcing[4]. Their overall 'sawtooth' structure consists of gradual global cooling and ice-volume build-up during glaciations, followed by rapid warming and melting during glacial terminations[4,9,13]. Millennial-scale episodes of North Atlantic cooling and ice-rafted-debris (IRD) deposition, commonly referred to as Heinrich events[14], punctuated each of the last five terminations[15,16]. During T-I, North Atlantic cooling and IRD events occurred during Heinrich Stadial 1 (HS1, ~18–14.6 kyr ago, ka) and the Younger Dryas (YD, ~12.8–11.5 ka), which coincided with weakened Atlantic Meridional Overturning Circulation (AMOC), drought in the boreal tropics, and heat build-up and strengthening of wind-driven upwelling in the Southern Ocean[1]. These developments were coupled with a bipolar temperature 'seesaw' and CO_2 release from the (Southern) ocean into the atmosphere[1]. Neither HS1 nor the YD appear to correspond to periods with high rates of deglacial sea-level rise[11] (so-called meltwater pulses, MWPs). This raises the question of whether the North Atlantic climate and sea-level change were decoupled only during T-I, or if this decoupling applied also to other terminations with different forcing histories. Accordingly, we need detailed assessments of the relative phasing between bipolar seesaw, atmospheric CO_2, and sea level through older terminations, while the absolute timing of these processes allows the resolution of their relationship with insolation forcing.

Absolute chronologies for terminations older than T-I hinge on radiometric (U-series) dating of speleothems and corals, while marine sediment cores lack such independent age control. Pioneering studies

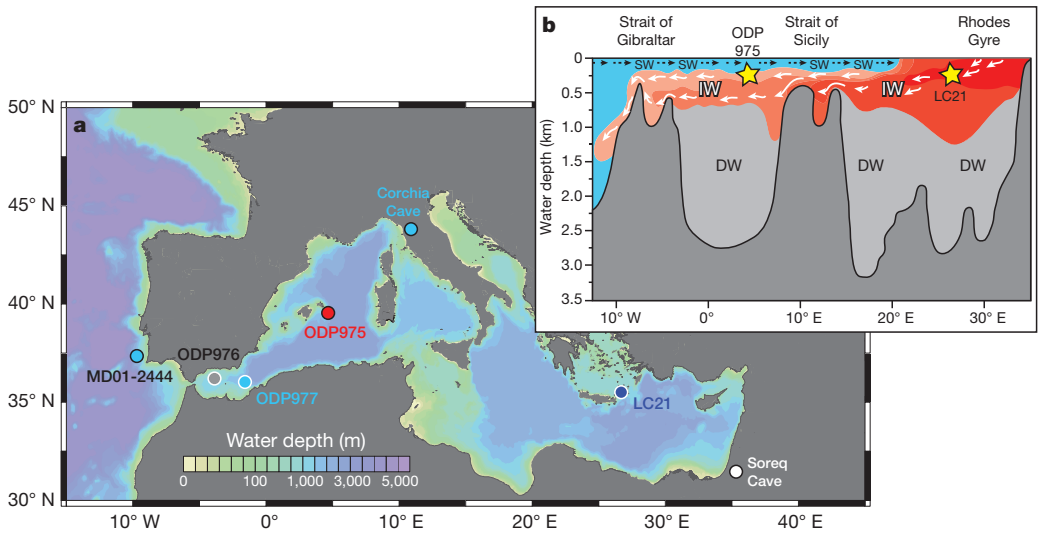

Figure 1 | Location of the palaeoclimate archives discussed here, and the Mediterranean circulation pattern. a, Bathymetric map of the Mediterranean Sea with locations of the marine and continental records discussed in the text. **b**, West–east cross-section across the Mediterranean Sea with a sketch of the basin's anti-estuarine circulation: surface inflow (black dashed arrows) through the Strait of Gibraltar and subsurface circulation and outflow (white arrows) into the Atlantic Ocean (Methods). Yellow stars indicate the upper intermediate-water depth habitat of *N. pachyderma* (d) (Methods) at the location of core LC21 (35° 40′ N, 26° 35′ E, water depth 1,522 m) and Ocean Drilling Program (ODP) Site 975 (38° 53.8′ N, 4° 30.6′ E, water depth 2,415 m). SW, surface water (blue); IW, intermediate-water (red); DW, deep water (grey).

[1]Research School of Earth Sciences, The Australian National University, Canberra, Australian Capital Territory 2601, Australia. [2]Ocean and Earth Science, University of Southampton, National Oceanography Centre, Southampton SO14 3ZH, UK. [3]Department of Geography, Wallace Building, Swansea University, Singleton Park, Swansea SA2 8PP, UK.

placed pre-T-I terminations on radiometrically constrained timescales using: (i) correlation between North Atlantic deep-sea benthic stable oxygen isotopes ($\delta^{18}O_{benthic}$) and coral sea-level benchmarks[17], (ii) inferred similarity between North Atlantic sea surface temperature (SST) and an Italian speleothem $\delta^{18}O$ ($\delta^{18}O_{speleothem}$) record interpreted in terms of precipitation change[7], and (iii) inferred synchronicity of North Atlantic cold events and Asian Monsoon weak episodes, archived in $\delta^{18}O_{speleothem}$ time series[16,18]. However, deep-sea hydrographic changes complicate interpretation of North Atlantic $\delta^{18}O_{benthic}$ records in terms of sea-level change[19], and factors other than precipitation may affect $\delta^{18}O_{speleothem}$ in the Mediterranean region[8]. Finally, the relationship between North Atlantic climate and Asian Monsoon intensity may not be straightforward on millennial timescales[20]. Hence, these studies laid critical foundations, but did not deliver a conclusive, quantitative (with uncertainties) chronological framework for pre-T-I terminations. Among these, T-II is noteworthy because its overall insolation forcing considerably exceeded that of T-I (Extended Data Fig. 1), and it culminated in an interglacial that was warmer than the Holocene[4,21], with sea level above present[4].

To advance the debate, we present a new radiometrically constrained chronology for North Atlantic records of climate variability across T-II and the last interglacial period. We use records that are co-registered in single sediment-sample series (that is, phase relationships are unambiguous), and well-understood land–sea climate relationships to transfer—with rigorous uncertainty propagation—radiometric (U-series) ages to marine records. We exploit the well-documented intermediate-water connectivity between the eastern and western Mediterranean Sea (Methods), and the relationship between marine surface water microfossil $\delta^{18}O$ and U-series-dated regional $\delta^{18}O_{speleothem}$ records[7,8] (Extended Data Fig. 2). We generated centennially resolved $\delta^{18}O$ and $\delta^{13}C$ records for Mediterranean surface- and intermediate-water dwelling planktic foraminifera *Globigerina bulloides* and *Neogloboquadrina pachyderma* (dextral) (Methods), respectively, from western Mediterranean Ocean Drilling Program (ODP) Site 975 (ODP975, Fig. 1). Next, we synchronized the ODP975 $\delta^{18}O_{N.\ pachyderma\ (d)}$ record to the $\delta^{18}O_{N.\ pachyderma\ (d)}$ record of eastern Mediterranean core LC21 (Fig. 2a; Methods). The latter was placed previously[8] on a radiometric timescale by relating its co-registered surface $\delta^{18}O$ signal to Soreq Cave $\delta^{18}O_{speleothem}$. Finally, we use the co-registered $\delta^{18}O_{G.\ bulloides}$ of ODP975 to further transfer the radiometrically constrained timescale to the $\delta^{18}O_{G.\ bulloides}$ record of nearby ODP Sites 976 (ODP976) and 977, and to core MD01-2444 and, in turn, to the SST and/or IRD records of North Atlantic climate variability that are archived in these sediment cores (Extended Data Figs 2, 3, Methods).

Comparison of $\delta^{18}O_{G.\ bulloides}$ from ODP975 and ODP976 on their new radiometrically constrained timescale with the Corchia Cave $\delta^{18}O_{speleothem}$ record on its own radiometric chronology (Methods) reveals a striking similarity with respect to both timing and magnitude of $\delta^{18}O$ shifts, notably between ~140 and ~129 ka (Fig. 2b). Possible correlation between western Mediterranean and Corchia Cave $\delta^{18}O$ signals was contemplated before[7], but—at that stage—an alternative coupling of North Atlantic warming with increased precipitation over central Italy was favoured. The two interpretations lead to substantially (up to ~4 kyr) different timings for HS11. The approach used here is independent of assumptions about the phasing between North Atlantic climate and $\delta^{18}O_{speleothem}$. Instead, it diagnostically indicates a source-water control on Corchia Cave $\delta^{18}O_{speleothem}$; negative $\delta^{18}O$ anomalies in North Atlantic and western Mediterranean surface waters—during Heinrich events[14] (see below)—were transmitted via the hydrological cycle to the cave catchment. The $\delta^{18}O$ similarity between ODP975 and Corchia Cave provides strong and independent validation of the LC21-based radiometric chronology for ODP975, and thus to the LC21–Soreq Cave synchronization used previously to provide radiometric age constraints to sea-level records[8]. Validation of the LC21–Soreq Cave synchronization was obtained using U-series-dated Asian monsoon records[9], so the T-II chronology

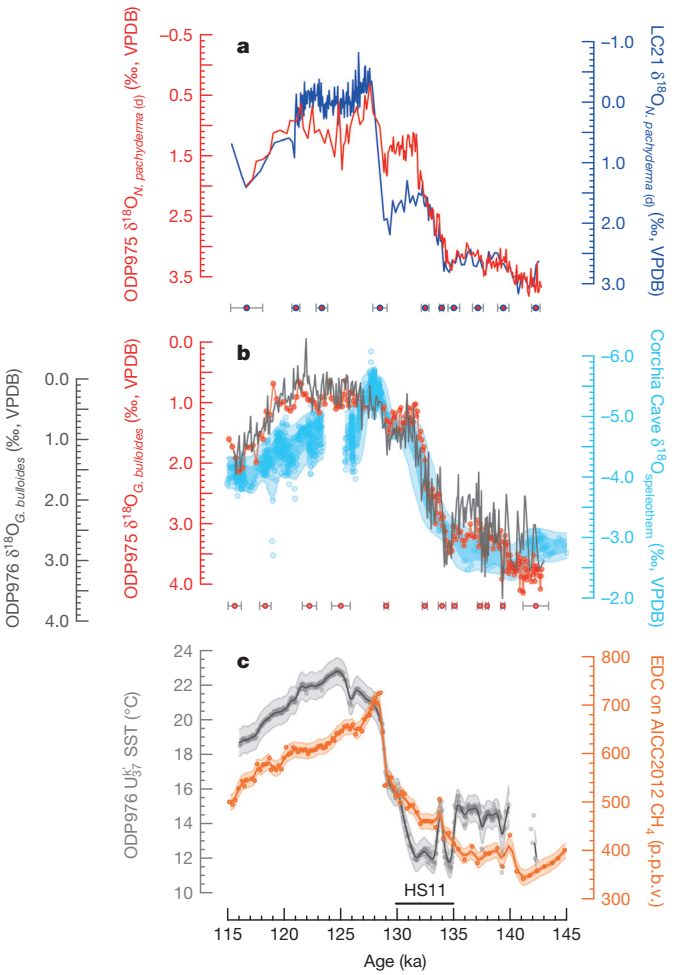

Figure 2 | Construction and validation of a radiometrically constrained chronology for western Mediterranean Sea ODP975 and ODP976. **a**, Synchronization of *N. pachyderma* (d) $\delta^{18}O$ from ODP975 (red line) to its counterpart from eastern Mediterranean core LC21 (blue line; Methods), which was placed on a radiometric chronology by ref. 8. Red filled circles and grey error bars depict the tie points used to synchronize ODP975 to LC21 and the 2σ synchronization uncertainties, respectively (Methods, Extended Data Table 1). **b**, Synchronization of *G. bulloides* $\delta^{18}O$ from ODP976 (grey line; after ref. 6) to its counterpart from nearby ODP975 (red line) on its radiometrically constrained chronology. Grey filled circles and error bars depict the tie points used to synchronize ODP976 to ODP975 and the 2σ synchronization uncertainties, respectively (Methods, Extended Data Table 2). Comparison of $\delta^{18}O_{G.\ bulloides}$ from ODP975 and ODP976 with the speleothem $\delta^{18}O$ ($\delta^{18}O_{speleothem}$) from Corchia Cave[7] (Italy) is made to validate (not to constrain) the chronology of the western Mediterranean cores. Confidence limits (95% lighter sky blue, 68% darker sky blue) for the Corchia Cave $\delta^{18}O_{speleothem}$ data (sky blue circles) result from Monte Carlo analysis (Methods) of the chronological and $\delta^{18}O_{speleothem}$ uncertainties (ref. 7). **c**, Comparison of the western Mediterranean ODP976 sea surface temperature (SST) data[6] (grey circles) on the radiometrically constrained chronology developed in this study with the Antarctic atmospheric methane (CH_4) record[23] (orange circles) on the AICC2012 timescale[22], supporting consistency between the two independent chronologies. Confidence limits for the ODP976 SST (95% light grey, probability maximum with 95% uncertainty, heavier grey line and envelope) and atmospheric CH_4 concentrations (95% light orange, probability maximum with 95% uncertainty, heavier orange line and envelope) result from Monte Carlo analysis of their chronological and proxy related uncertainties, employing Gaussian filters of 0.2 and 0.4 kyr, respectively (Methods). Black bar indicates the timing of Heinrich Stadial 11 (HS11).

of sea-level change now involves agreement between three independent, radiometrically constrained approaches.

Investigation of the interhemispheric climate relationships requires first an assessment of consistency between our new radiometrically

constrained chronology and the AICC2012 timescale for the Antarctic EPICA Dome C (EDC) ice core[22]. Building on the notion that atmospheric methane (CH_4) concentrations and Greenland/North Atlantic temperatures covaried on millennial timescales[23], we compare the western Mediterranean SST record (reflecting North Atlantic climate[6]) on our new chronology with the EDC CH_4 record[23] on AICC2012 (Fig. 2c). The remarkable signal similarity between 131 and 128 ka supports consistency between the two independent chronologies across this interval. Such consistency plausibly extends back to ~134 ka, when a distinct SST maximum coincided with a CH_4 peak. Although the latter is documented by a single data point in EDC, the Vostok Antarctic ice core CH_4 record[24] appears to corroborate the occurrence of a CH_4 peak at this time.

In the following we examine in millennial-scale detail the relative timing between insolation, North Atlantic climate, sea level, Antarctic temperatures, and atmospheric CO_2 across HS11 and the transition into the last interglacial period (Fig. 3a–f). T-II contains two major meltwater pulses[9] (MWP-2A and MWP-2B), which are centred on 139 ± 1 and 133 ± 1 ka (2σ uncertainties[8]) and coincided within uncertainties with two North Atlantic cooling episodes (Fig. 3c, d). MWP-2A indicates an early phase of ice-sheet retreat. Similar to its T-I counterpart[3] at ~19 ka, it coincided with a short-lived (~2 °C) North Atlantic cooling. MWP-2B is more convincingly resolved and marks a steep ~70 m sea-level rise (~70% of the glacial–interglacial change) at rates of 28 ± 8 m kyr^{-1} (refs 8, 9). It lagged 4 ± 1 kyr behind the boreal summer insolation rise and coincided with the prominent North Atlantic cold phase, HS11 (Fig. 3b–d). Our new chronology places the initiation and termination of HS11 at 135 ± 1 and 130 ± 2 ka (2σ uncertainties), respectively, and the ~0.5-kyr warm interlude[6] that briefly interrupted it at 134 ± 1 ka (Fig. 3c), in overall agreement with the 'synthetic' Greenland record[16] (Extended Data Fig. 3). HS11 also coincided with over half of the glacial–interglacial atmospheric CO_2 increase, and with ~9 °C Antarctic warming[13] (Fig. 3e, f). Only ~5 °C of this warming can be ascribed to radiative forcing[21], which leaves ~4 °C of 'residual' warming that we interpret as the Southern Ocean bipolar temperature seesaw response[12] to meltwater-forced AMOC collapse and attendant North Atlantic cooling (Fig. 3c, d).

An intense seesaw response with strong North Atlantic cooling suggests that the meltwater entered the North Atlantic. This inference is supported by major North Atlantic IRD deposition (Fig. 3b), the large magnitude (~70 m) sea-level rise associated with MWP-2B (maximum freshwater flux of 0.3 ± 0.04 Sv; Fig. 4a) that requires intense reduction of the large northern ice-sheets, and the distinct source-water-related negative shift in $\delta^{18}O$ of precipitation ($\Delta\delta^{18}O_{precipitation}$) at Corchia Cave (Fig. 4b), interpreted here as a reflection of meltwater-based freshening of the wider North Atlantic (Methods). The seesaw response at the time of HS11 is also corroborated by its agreement with the established relationship between magnitudes of Antarctic warming and North Atlantic stadial duration during the last glacial cycle (Extended Data Fig. 4). Finally, HS11 coincided with a weak Asian monsoon event[18] and South American monsoon intensification[25], both archived in radiometrically dated speleothems and interpreted in terms of a southward shift of the Intertropical Convergence Zone (ITCZ) in response to AMOC weakening. The relative timing between ITCZ dynamics, AMOC, and North Atlantic climate is well documented across T-I and within the

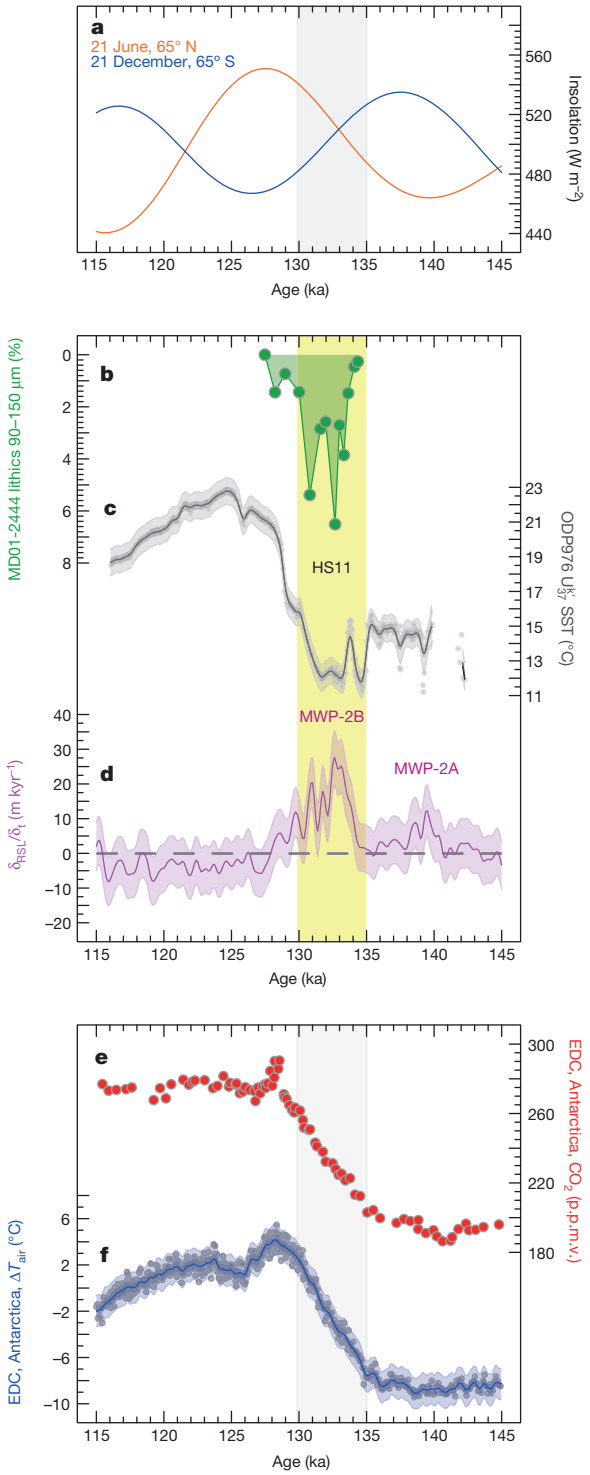

Figure 3 | Interhemispheric records of climate change across glacial Termination II. **a**, Boreal and austral summer insolation curves; age is calculated using astronomical solutions[31]. **b**, Ice-rafted-debris (IRD) record from core MD01-2444, Iberian Margin[19] (North Atlantic). **c**, Sea surface temperature (SST) record from ODP976, western Mediterranean Sea[6]. The 95% confidence limits (light grey envelope) and probability maximum (heavier grey line) with 95% uncertainty (heavier grey envelope) of the SST data (grey circles) are based on a Monte Carlo analysis of chronological and SST uncertainties, employing a 0.2 kyr Gaussian filter (Methods). Profiles in **b** and **c** are on the radiometrically constrained chronology developed in this study (Methods). **d**, Rates of relative sea-level change (δ_{RSL}/δ_t) with associated 95% confidence limits (magenta shaded envelopes) of the probability maximum (magenta solid line) from Monte Carlo analysis of uncertainties in the relative sea-level reconstructions and chronology[9]. **e**, Composite atmospheric CO_2 concentrations from EPICA Dome C (EDC) (Methods). **f**, Antarctic air temperatures[13] (ΔT_{air}) from EDC. The 95% confidence limits (light blue envelope) and probability maximum (heavier blue line) and its associated 95% uncertainty (heavier blue envelope) for the ΔT data (blue circles) are based on a Monte Carlo analysis of chronological and ΔT uncertainties, employing a 0.2 kyr Gaussian filter (Methods). Data in **e** and **f** are plotted on the AICC2012 timescale[22] (Methods). HS11, Heinrich Stadial 11; MWP, meltwater pulse.

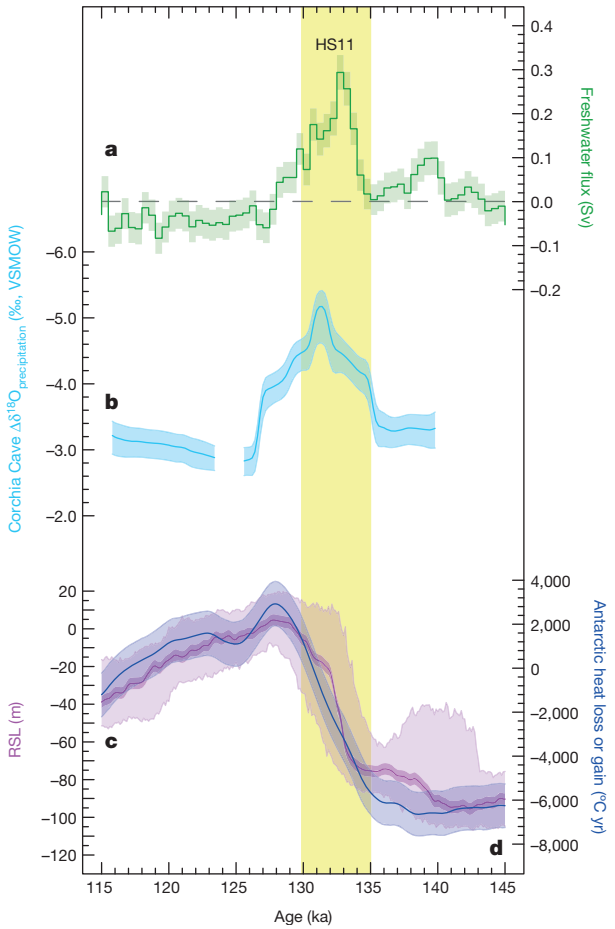

Figure 4 | Origin and impacts of meltwater pulses during glacial termination II. **a**, Freshwater fluxes calculated (Supplementary Information) from rates of sea-level change[9]. **b**, Ice-volume and temperature corrected $\delta^{18}O$ of Corchia Cave speleothem (Methods), indicating isotopic anomalies of precipitation in the cave catchment. Envelopes are the 95% confidence limits of the probability maximum (solid line) obtained from a Monte Carlo approach that takes into account proxy related and chronological uncertainties of the various records (Methods). **c**, Relative Sea Level (RSL)[9]. The 95% confidence limits (light magenta) and the probability maximum with 95% uncertainty (heavy magenta line and shading) were presented in ref. 9. **d**, Antarctic heat loss/gain obtained by integrating the Antarctic temperatures[13] over a period of 0.75 ± 0.15 kyr, using a Monte Carlo approach employing a 0.8 kyr Gaussian filter of the data (blue).

last glacial cycle[26]. Similar scenarios were suggested for previous terminations[18] (including T-II), but required assumptions about timing relationships between records. By placing all records on a single radiometrically constrained chronology, our results overcome this limitation, and independently corroborate the scenario for T-II.

Since ~70% of the glacial–interglacial sea-level rise (MWP-2B) occurred during a phase of weak AMOC (HS11; Fig. 3b–d), T-II fundamentally differed from T-I. During T-I, ~75% of the sea-level rise[11] post-dated the major deglacial cooling phase in the North Atlantic (HS1), and the largest meltwater pulse (MWP-1A; 15–20% of the deglacial sea-level rise) peaked when the North Atlantic was warm (or warming) and AMOC was relatively strong (or strengthening)[3,10,27]. This fuelled arguments that Antarctic ice sheets contributed substantially to MWP-1A (ref. 10). In contrast, we find that MWP-2B was more than three times larger than MWP-1A, and was tied directly to circum-North-Atlantic ice-sheet reduction and attendant North Atlantic cooling. This fundamentally different relationship between North Atlantic climate and sea-level change during the last two terminations indicates that during T-II, Northern Hemisphere ice sheets collapsed early in the termination, possibly in response to a combination of overall stronger (and more rapidly rising[18]) boreal summer insolation and higher atmospheric CO_2 (Extended Data Fig. 1).

Our reconstructed phasing of interhemispheric climate developments through HS11 is consistent with a southward shift and/or possible strengthening of Southern Ocean westerlies[28], and associated subsurface oceanic warming around Antarctica[29]. This provides a mechanism for conveying the oceanic heat related to the bipolar seesaw to Antarctica. The attendant excess warming of ~4 °C in Antarctica[21] (see above) during HS11 would have then affected the Antarctic ice sheet stability through processes such as under-ice melting and grounding line retreat of ice-shelves[30]. To account for relatively long (but poorly known) adjustment timescales of this major ice sheet to warming, including the excess 4 °C, we approximate heat gain/loss by integrating the Antarctic temperature record over time[13]. We find that the timings of maximum heat gain and the last interglacial sea-level peak[8] match best for an overall integration timescale of 0.75 ± 0.15 kyr (Fig. 4c).

Securing records to a single, radiometrically constrained chronology reveals the sequence of events through T-II. An initial (minor but significant) ice-sheet reduction caused MWP-2A during a Northern Hemisphere insolation minimum. Next followed the main phase of northern ice-sheet reduction (MWP-2B), ~4 kyr after the onset of insolation rise, which caused AMOC collapse, with attendant North Atlantic cooling and (seesaw) Southern Ocean warming. We infer that resultant Antarctic heating drove continuation of sea-level rise well after MWP-2B, up to several metres above present[4], which predominantly reflects Antarctic ice reduction.

Online Content Methods, along with any additional Extended Data display items and Source Data, are available in the online version of the paper; references unique to these sections appear only in the online paper.

Received 26 November 2014; accepted 15 April 2015.

1. Denton, G. H. *et al.* The last glacial termination. *Science* **328,** 1652–1656 (2010).
2. Clark, P. U. *et al.* Global climate evolution during the last deglaciation. *Proc. Natl Acad. Sci. USA* **109,** E1134–E1142 (2012).
3. Carlson, A. E. & Clark, P. U. Ice sheet sources of sea level rise and freshwater discharge during the last deglaciation. *Rev. Geophys.* **50,** RG4007 (2012).
4. Masson-Delmotte, V. *et al.* in *Climate Change 2013: The Physical Science Basis* (eds Stocker, T. F.) Ch. 5 383–464 (Cambridge Univ. Press, 2013).
5. Oppo, D. W., McManus, J. F. & Cullen, J. L. Evolution and demise of the Last Interglacial warmth in the subpolar North Atlantic. *Quat. Sci. Rev.* **25,** 3268–3277 (2006).
6. Martrat, B., Jimenez-Amat, P., Zahn, R. & Grimalt, J. O. Similarities and dissimilarities between the last two deglaciations and interglaciations in the North Atlantic region. *Quat. Sci. Rev.* **99,** 122–134 (2014).
7. Drysdale, R. N. *et al.* Evidence for obliquity forcing of glacial termination II. *Science* **325,** 1527–1531 (2009).
8. Grant, K. M. *et al.* Rapid coupling between ice volume and polar temperature over the past 150,000 years. *Nature* **491,** 744–747 (2012).
9. Grant, K. M. *et al.* Sea-level variability over five glacial cycles. *Nature Commun.* **5,** 5076 (2014).
10. Clark, P. U., Mitrovica, J. X., Milne, G. A. & Tamisiea, M. E. Sea-level fingerprinting as a direct test for the source of global meltwater pulse IA. *Science* **295,** 2438–2441 (2002).
11. Lambeck, K., Rouby, H., Purcell, A., Sun, Y. & Sambridge, M. Sea level and global ice volumes from the Last Glacial Maximum to the Holocene. *Proc. Natl Acad. Sci. USA* **111,** 15296–15303 (2014).
12. Stocker, T. F. & Johnsen, S. J. A minimum thermodynamic model for the bipolar seesaw. *Paleoceanography* **18,** 1087 (2003).
13. Jouzel, J. *et al.* Orbital and millennial Antarctic climate variability over the past 800,000 years. *Science* **317,** 793–796 (2007).
14. Hemming, S. R. Heinrich events: massive late Pleistocene detritus layers of the North Atlantic and their global climate imprint. *Rev. Geophys.* **42,** RG1005 (2004).
15. McManus, J. F., Oppo, D. W. & Cullen, J. L. A 0.5-million-year record of millennial-scale climate variability in the North Atlantic. *Science* **283,** 971–975 (1999).
16. Barker, S. *et al.* 800,000 years of abrupt climate variability. *Science* **334,** 347–351 (2011).
17. Shackleton, N. J., Sanchez-Goni, M. F., Pailler, D. & Lancelot, Y. Marine isotope substage 5e and the Eemian interglacial. *Glob. Planet. Change* **36,** 151–155 (2003).
18. Cheng, H. *et al.* Ice age terminations. *Science* **326,** 248–252 (2009).
19. Skinner, L. C. & Shackleton, N. J. Deconstructing Terminations I and II: revisiting the glacioeustatic paradigm based on deep-water temperature estimates. *Quat. Sci. Rev.* **25,** 3312–3321 (2006).

20. Rohling, E. J. *et al.* Controls on the East Asian monsoon during the last glacial cycle, based on comparison between Hulu Cave and polar ice-core records. *Quat. Sci. Rev.* **28,** 3291–3302 (2009).
21. Masson-Delmotte, V. *et al.* EPICA Dome C record of glacial and interglacial intensities. *Quat. Sci. Rev.* **29,** 113–128 (2010).
22. Bazin, L. *et al.* An optimized multi-proxy, multi-site Antarctic ice and gas orbital chronology (AICC2012): 120–800 ka. *Clim. Past.* **9,** 1715–1731 (2013).
23. Loulergue, L. *et al.* Orbital and millennial-scale features of atmospheric CH_4 over the past 800,000 years. *Nature* **453,** 383–386 (2008).
24. Delmotte, M. *et al.* Atmospheric methane during the last four glacial-interglacial cycles: Rapid changes and their link with Antarctic temperature. *J. Geophys. Res. D* **109,** D12104 (2004).
25. Wang, X. F. *et al.* Wet periods in northeastern Brazil over the past 210 kyr linked to distant climate anomalies. *Nature* **432,** 740–743 (2004).
26. Schneider, T., Bischoff, T. & Haug, G. H. Migrations and dynamics of the intertropical convergence zone. *Nature* **513,** 45–53 (2014).
27. Weaver, A. J., Saenko, O. A., Clark, P. U. & Mitrovica, J. X. Meltwater pulse 1A from Antarctica as a trigger of the Bølling-Allerød warm interval. *Science* **299,** 1709–1713 (2003).
28. Toggweiler, J. R., Russell, J. L. & Carson, S. R. Midlatitude westerlies, atmospheric CO_2, and climate change during the ice ages. *Paleoceanography* **21,** PA2005 (2006).
29. Spence, P. *et al.* Rapid subsurface warming and circulation changes of Antarctic coastal waters by poleward shifting winds. *Geophys. Res. Lett.* **41,** 4601–4610 (2014).
30. Joughin, I., Alley, R. B. & Holland, D. M. Ice-sheet response to oceanic forcing. *Science* **338,** 1172–1176 (2012).
31. Laskar, J. *et al.* A long-term numerical solution for the insolation quantities of the Earth. *Astron. Astrophys.* **428,** 261–285 (2004).

Supplementary Information is available in the online version of the paper.

Acknowledgements We thank the International Ocean Discovery Program for providing samples from Leg 161 and W. Hale for sampling assistance. M. Charidemou contributed to a pilot study on ODP975, J. Amies to preliminary stratigraphic assessment, and J. Cali to stable isotope analyses. We thank M. Bar-Matthews for providing the updated version of the Soreq Cave chronology table, R. N. Drysdale and J. Hellstrom for helpful discussions, and B. Martrat and L. Skinner for making published data available. This study was supported by Australian Research Council Australian Laureate Fellowship FL120100050 and by UK-NERC project NE/I009906/1 (E.J.R.).

Author Contributions G.M. and E.J.R. designed the study. G.M. prepared the foraminiferal samples for stable isotope analyses and together with E.J.R. and D.H. performed the statistical analysis. L.R.S. performed the stable isotope analyses. K.M.G. and J.D.S. oversaw early stratigraphic assessment. All authors contributed to interpretation and preparation of the final manuscript.

Author Information Reprints and permissions information is available at www.nature.com/reprints. The authors declare no competing financial interests. Readers are welcome to comment on the online version of the paper. Correspondence and requests for materials should be addressed to G.M. (Gianluca.Marino@anu.edu.au).

METHODS

Core material. Ocean Drilling Program (ODP) Site 975 was drilled by RV *Joides Resolution* in the western Mediterranean Sea (Fig. 1; 38° 53.8′ N, 4° 30.6′ E; water depth 2,415 m). ODP Site 975 is located on the Menorca Rise[32], along the path of the Atlantic surface water entering the Mediterranean Sea through the Strait of Gibraltar and flowing eastward across the basin[33–36]. Sections 2H4 to 2H6 from ODP Site 975 Hole C were sampled using u-channels, and subsequently sliced at 1 cm resolution. Data were generated for this study at a resolution of 1 to 2 cm.

Stable oxygen ($\delta^{18}O$) and carbon ($\delta^{13}C$) isotopes. For ODP Site 975, 20–30 individuals of *G. bulloides* (300–355 μm size fraction) and 10–20 individuals of *N. pachyderma* (d) (212–250 μm size fraction) were picked. For core LC21, 10–15 individuals of *N. pachyderma* (d) (250–300 μm size fraction) were picked to increase the resolution and spliced together with previously published records[8,37] between 143 and 129 ka. To avoid complications arising from size-dependent vital effects in planktic foraminifera[38,39], we constrained the size window of the picked foraminifera from ODP Site 975 and core LC21 to a maximum of ~55 μm. This compromised the continuity of the *G. bulloides* $\delta^{18}O$ and $\delta^{13}C$ records between 129 and 127 ka in ODP Site 975, as *G. bulloides* abundance drops significantly in that interval, and insufficient numbers were available in one strict size window.

Prior to analysis, foraminiferal samples were crushed, cleaned and ultrasonicated briefly in methanol. The cleaned samples were then analysed ($\delta^{18}O$ and $\delta^{13}C$) at the Australian National University with a Thermo Finnigan Delta Advantage mass spectrometer coupled to a Kiel IV carbonate device, in which samples react with 105% phosphoric acid at 75 °C. Results were normalized to the Vienna Peedee Belemnite (VPDB) scale with the NBS-19 ($\delta^{18}O = -2.20‰$, $\delta^{13}C = 1.95‰$) and NBS-18 ($\delta^{18}O = -23.20‰$, $\delta^{13}C = -5.014‰$) carbonate standards. External reproducibility (1σ) of a carbonate standard (NBS-19) was better than ±0.08‰ for $\delta^{18}O$ and ±0.06‰ for $\delta^{13}C$.

Chronology for ODP Site 975. Synchronization of western Mediterranean ODP Site 975 to eastern Mediterranean core LC21 exploits the strong oceanographic connectivity between the two Mediterranean sub-basins at intermediate depths. Vigorous intermediate circulation transports water westward from the Rhodes Gyre (nearby core LC21, Fig. 1), to the western Mediterranean, and eventually through the Strait of Gibraltar as Mediterranean outflow into the Atlantic Ocean (for example, refs 33–36). Data[40] and numerical modelling[41] indicate that this intermediate-water connection is an enduring feature of Mediterranean circulation through time. Accordingly, characterization of past geochemical property changes in intermediate waters across the Mediterranean provides a valuable tool for synchronizing sediment cores from different sectors of the basin. To characterize variability of the intermediate waters at ODP Site 975 and core LC21, we use new (see above) and existing[8,37] $\delta^{18}O$ and $\delta^{13}C$ data for the upper intermediate-water dwelling[38] planktic foraminifer *N. pachyderma* (d).

Based on the enduring intermediate-water connection, the $\delta^{18}O_{N.\ pachyderma\ (d)}$ profile of ODP Site 975 is synchronized with that of LC21 (Fig. 2a, Extended Data Figs 2, 5), for which a radiometrically constrained chronology was recently developed, based on a strong surface-water $\delta^{18}O$ relationship with $\delta^{18}O$ in speleothems ($\delta^{18}O_{speleothem}$) in Soreq Cave (Israel)[8]. Specifically, we identified ten $\delta^{18}O_{N.\ pachyderma\ (d)}$ shifts, each represented by multiple (ranging from 3 to 34) data points, and used their mid-points to place the ODP Site 975 records onto the LC21 chronology of ref. 8 (Fig. 2a, Extended Data Fig. 5a). We linearly interpolated ages between age control points, assuming constant sedimentation rates between them. We adopted this approach because there is no evidence to suggest highly variable sedimentation rates at ODP Site 975. In addition, this assumption does not affect the age of the individual tie-points and hence our conclusions, given that the timing of HS11 is constrained by four age control points.

The ODP Site 975 and LC21 $\delta^{18}O_{N.\ pachyderma\ (d)}$ profiles are virtually identical between ~143 and ~132 ka. An abrupt shift to lighter values at ~132 ka follows at ODP Site 975, while it is not observed in LC21. Next, the ODP Site 975 $\delta^{18}O_{N.\ pachyderma\ (d)}$ stabilizes at values of ~1.6‰ before shifting again at 129 ka (as does its LC21 counterpart) to reach a distinct minimum 128 kyr ago. The interval between 132 and 130 ka coincides with the strongest phase of Heinrich Stadial 11, when, according to our analysis, the meltwater discharge into the North Atlantic Ocean reached its maximum (see main text). This delivered large volumes of isotopically light freshwater to the North Atlantic and (via the Strait of Gibraltar) to the western Mediterranean Sea. Similar to (smaller) events during the last glacial cycle[42], such influxes would have affected intermediate levels of the water column, for example, through winter mixing in the northwestern Mediterranean[43], where ODP Site 975 is located (Fig. 1). Between 128 and 121 ka, the ODP Site 975 and LC21 $\delta^{18}O_{N.\ pachyderma\ (d)}$ records diverge somewhat (although both become more positive at 126–123 ka). This is probably due to enhanced stratification in the eastern Mediterranean during the monsoon-related freshwater inputs along the North African Margin[36–38,44–46]. From ~121 to ~117 ka, there is a similar magnitude positive shift in the ODP Site 975 and LC21 $\delta^{18}O_{N.\ pachyderma\ (d)}$ records.

Our inferred synchronization of marine sediment records and the accuracy of the radiometrically constrained chronology we derived for ODP Site 975 can be independently validated (Extended Data Fig. 2). First, we did not use the $\delta^{13}C_{N.\ pachyderma\ (d)}$ profiles for ODP975 and core LC21 to constrain the synchronization between the two sites but use those data on the synchronized age model for validation purposes (Extended Data Fig. 5b). There is a remarkable agreement between the ODP975 and LC21 $\delta^{13}C_{N.\ pachyderma\ (d)}$ profiles particularly between 129 and 126 ka and between 123 and 120 ka, when both records have considerably lighter values than in the preceding glacial and deglacial periods (Extended Data Fig. 5b). The $\delta^{13}C_{N.\ pachyderma\ (d)}$ minimum is a characteristic feature of intervals of sapropel deposition in the eastern Mediterranean and testifies to subsurface accumulation of isotopically light respiration products in response to decreased deep sea ventilation[36–38,45,47]. With an isotopic shift in excess of −3‰, this feature is particularly prominent during last interglacial sapropel S5 (ref. 38), which is well-documented[37,46,48,49] and precisely dated[8] (~128 to ~121 ka) in core LC21. Contemporaneous $\delta^{13}C_{N.\ pachyderma\ (d)}$ minima in both core LC21 and ODP Site 975 during S5, therefore, supports our synchronization, in that they indicate that a low-$\delta^{13}C$ anomaly has been effectively transferred via intermediate waters from the eastern to the western Mediterranean basin, in line with previous studies[40]. The ~2 kyr shift to heavier $\delta^{13}C_{N.\ pachyderma\ (d)}$ values between 126 and 124 ka at ODP Site 975 reflects an interval of potentially weakened sapropel conditions in the eastern Mediterranean during which deep-sea ventilation may have intermittently resumed[37,44,45] and the transport of low-$\delta^{13}C$ water to the western basin interrupted. Second, between 140 and 129 ka there is a strong similarity between changes in the ODP Site 975 $\delta^{18}O_{G.\ bulloides}$ and $\delta^{18}O_{speleothem}$ from Corchia Cave (Fig. 2b). This indicates that the large negative shift in the $\delta^{18}O_{speleothem}$ between ~135 and ~130 ka resulted mostly from a ^{18}O-depletion of similar magnitude in the source of precipitation for Corchia, which at present[50] and on glacial–interglacial timescales[51] is the wider North Atlantic Ocean/western Mediterranean Sea. Note that source water influence on $\delta^{18}O_{speleothem}$ is a common feature of the Mediterranean cave records[8,36,52,53]. This interpretation is further corroborated by the fact that increase in speleothem growth rates and decrease in speleothem $\delta^{13}C$ did not occur before ~130 ka[7] and by a similarly timed growth rate increase in a nearby cave[54]. Concurrence of these climate signals in the mid-latitude speleothems indicates a transition from drier/colder to wetter/warmer conditions[7] that therefore occurred at the end of the large negative $\delta^{18}O_{speleothem}$ shift, that is, after 130 ka.

Chronology for ODP Sites 976 and 977 and core MD01-2444. The $\delta^{18}O_{G.\ bulloides}$ record for core ODP Site 975 is used to transfer our new radiometrically constrained chronology of ODP Site 975 to $\delta^{18}O_{G.\ bulloides}$ in other western Mediterranean (ODP Sites 976 and 977) and Iberian Margin (North Atlantic, MD01-2444) sediment cores (Fig. 2b, Extended Data Figs 2, 3a, c). Alignment of co-registered (same sample series) alkenone-based sea surface temperature (SST) records from ODP Site 977 and core MD01-2444 with that from ODP Site 976 lends credence to the robustness of the $\delta^{18}O_{G.\ bulloides}$-based synchronization (Extended Data Fig. 5b, d).

Propagation of chronological uncertainties. Propagation of chronological uncertainties through the various synchronization steps used in this study to transfer the chronology of core LC21 (ref. 8) to ODP Site 975 and then to ODP Site 976, ODP Site 977, and core MD01-2444 follows the exact same approach used by Grant *et al.* (ref. 8). The steps are outlined below.

(i) From core LC21 to ODP Site 975. For LC21 the chronological uncertainty at each depth level was obtained by linearly interpolating the uncertainties between the tie-points used for transferring the radiometric chronology of Soreq Cave to LC21 (ref. 8). Next we calculate root-mean-square errors (MSE) that propagate all the chronological uncertainties involved in the synchronization of ODP Site 975 to LC21. Specifically, we include the dating error associated with the LC21 chronology of Grant *et al.* (ref. 8), the sample spacing of the $\delta^{18}O_{N.\ pachyderma\ (d)}$ record in core LC21, the sample spacing of $\delta^{18}O_{N.\ pachyderma\ (d)}$ in ODP Site 975, and extra uncertainty (2 or 3 times the sample spacing) for more ambiguous tie-points (indicated in red in the Extended Data Table 1).

(ii) From ODP Site 975 to ODP Site 976. For ODP Site 975, the chronological uncertainty at each depth level was obtained by linearly interpolating the uncertainties between the tie-points used for transferring the radiometrically constrained chronology of LC21 to ODP Site 975. Next we use MSE that propagate all the chronological uncertainties involved in the synchronization of ODP Site 975 to ODP Site 976. This includes the ODP Site 975 chronological uncertainty from (i), the sample spacing of $\delta^{18}O_{G.\ bulloides}$ in ODP Site 975, the sample spacing of $\delta^{18}O_{G.\ bulloides}$ in ODP Site 976, and extra uncertainty (2 or 3 times the sample spacing) for more ambiguous tie-points (Extended Data Table 2).

(iii) From ODP Site 975 to ODP Sites 977. We include the ODP Site 975 chronological uncertainty (as reported in (ii)), the sample spacing of $\delta^{18}O_{G.\ bulloides}$ in ODP Site 975, the sample spacing of $\delta^{18}O_{G.\ bulloides}$ in ODP Site 977, and extra uncertainty (2 or 3 times the sample spacing) for more ambiguous tie-points. These uncertainties were propagated as root-mean-square errors (MSE) (Extended Data Table 3).

(iv) From ODP Site 975 to core MD01-2444. We include the ODP Site 975 chronological uncertainty from (as reported in (ii)), the sample spacing of $\delta^{18}O_{G.\ bulloides}$ in ODP Site 975, the sample spacing of $\delta^{18}O_{G.\ bulloides}$ in core MD01-2444, and extra uncertainty (2 or 3 times the sample spacing) for more ambiguous tie-points. These uncertainties were propagated as root-mean-square errors (MSE) (Extended Data Table 4).

Records of atmospheric CO_2 and CH_4 and Antarctic temperatures. Existing records of atmospheric CO_2 and CH_4 concentrations and Antarctic atmospheric temperatures were placed on the latest ice-core chronology (AICC2012)[22,55]. For atmospheric CO_2 concentrations (Fig. 3e), a composite was made of the records by Landais *et al.* (ref. 56) and Schneider *et al.* (ref. 57).

Probabilistic assessment of the time series. We performed a probabilistic assessment of uncertainties for several of the new and previously published proxy records discussed in our study (for example, Figs 2b, c, 3c, f) in order to evaluate their confidence levels, taking into full account the uncertainties associated with both their chronologies (X) and proxy measurements/calibrations (Y). This analysis of the time series relies on Monte Carlo-style simulations of the input data using MATLAB. For each time series, all individual data points are separately and randomly sampled 10,000 times within their X- and Y-uncertainties. The 'Y-uncertainties', related to the proxy reconstructions (for example, sea surface temperature), are taken from the original source (for example, Martrat *et al.*, refs 6, 58, 59). The 'X-uncertainties', related to the chronologies of the various records, are either taken from the error propagation discussed above (Mediterranean and North Atlantic records) or from the original source (Corchia Cave[7], sea-level[8,9], and Antarctic ice core records[22,55]). Each of the 10,000 iterations was then either linearly interpolated (for example, Fig. 2b) or smoothed using a Gaussian filter of defined time window (for example, Fig. 2c). Next, the probability distribution of the 10,000 iterations was assessed per time step, which allowed determination of the 68% (16th–84th percentile) and 95% (2.5th–97.5th percentile) probability intervals for the data. Finally, we determined the probability maximum (modal value) at each time step, and its uncertainties (notably, the 95% probability interval for the probability maximum). For details on this approach, see refs 8, 60.

Calculation of freshwater fluxes from rates of sea-level change. *Code availability.* Freshwater fluxes shown in Fig. 4a were calculated from rates of sea-level change[9], using a script that was developed in MATLAB and is available in the Supplementary Information.

Relationships between sea level and seawater oxygen isotopes. The response of $\delta^{18}O$ in planktic foraminifera from the eastern Mediterranean Sea to sea-level change has recently been quantified[60]. This builds on the notion that sea level controls water exchange between the Mediterranean Sea and the Atlantic Ocean through the Strait of Gibraltar and, in turn, the residence time of waters in the basin[60–62]. Because of the highly evaporative conditions over the Mediterranean region, a longer residence time of water leads to higher salinity and $\delta^{18}O$ of seawater, which is, in turn, archived in the $\delta^{18}O$ of foraminiferal calcite[38,60,62]. Here we use results from the model of ref. 60 to decipher the 'glacial ^{18}O-enrichment' in eastern Mediterranean seawater, which is approximated by a second-order polynomial regression (Extended Data Fig. 6). Note that the generous uncertainties associated with the regression are mostly systematic[60] and therefore have minor impacts on the relative seawater $\delta^{18}O$ ($\delta^{18}O_{seawater}$) shifts assessed here. Next, we (re)calculate the relationship between sea-level lowering and mean open-ocean $\delta^{18}O_{seawater}$ due to freshwater loss from the ocean to the continental ice sheets during glacial times. This was done before[63], but here we use the latest sea-level assessment for the last glacial maximum[11] (LGM) and the contemporaneous oceanic $\delta^{18}O_{seawater}$ value reconstructed from pore water analyses of deep-sea cores[63]. Finally, we evaluate the response of western Mediterranean $\delta^{18}O_{seawater}$ to sea-level change by employing a linear mixing model of the open ocean ($30 \pm 5\%$) and eastern Mediterranean ($70 \pm 5\%$) end-members at each sea-level value that probabilistically evaluates the uncertainties in the various regressions. This mixing ratio is consistent with the range of salinity gradients across the Mediterranean Sea under present-day and LGM boundary conditions[64].

Corchia Cave palaeoprecipitation $\delta^{18}O$ changes and source-water effect. To obtain a time series of the $\delta^{18}O$ anomaly of precipitation ($\Delta\delta^{18}O_{precipitation}$) in the catchment area of Corchia Cave between 145 and 115 ka (shown in Fig. 4b), we 'deconstructed' the $\delta^{18}O_{speleothem}$ into its main components. These include the cave temperature that controls the isotopic fractionation between dripping water and inorganic (speleothem) calcite[65,66] and the $\delta^{18}O$ of precipitation ($\delta^{18}O_{precipitation}$). The latter reflects the interplay of two independent factors: (i) the $\delta^{18}O$ of the mean marine source of precipitation, for which variability depends on the glacial ^{18}O-enrichment (see above), and (ii) the residual, here referred to as $\Delta\delta^{18}O_{precipitation}$ component, which reflects variations in the isotopic composition of precipitation either due to inputs of isotopically light freshwater to the North Atlantic and (via Gibraltar) to the western Mediterranean Sea (for example, from melting ice sheets) or due to changes in the amount of precipitation[67].

Our approach relies on the assumption that the temperature change within the cave reflects mean annual temperature changes in the regional climate[7], as reflected in the western Mediterranean SST. We also consider the propagated chronological uncertainties of the three records used to derive the $\Delta\delta^{18}O_{precipitation}$ time series. To probabilistically evaluate the impacts of these assumptions and uncertainties on $\Delta\delta^{18}O_{precipitation}$, we have used a Monte Carlo approach (see above), in which the SST record[6], the sea-level driven mean ocean $\delta^{18}O_{seawater}$, and $\delta^{18}O_{speleothem}$ from Corchia Cave are given as input data along with the propagated chronological uncertainties. Note that calculation of the $\Delta\delta^{18}O_{precipitation}$ using a glacial mean ocean ^{18}O-enrichment and a western Mediterranean ^{18}O-enrichment are statistically indistinguishable across the interval of interest. This analysis is possible here for the first time because we placed all relevant records on the same timescale with rigorous assessment of the propagated uncertainties.

The negative $\Delta\delta^{18}O_{precipitation}$ shift in Corchia Cave during HS11 had a magnitude of ~1.5‰ (Fig. 4b). An order of magnitude mass-balance assessment suggests that a ^{18}O-depletion by 1.5‰ in the wider North Atlantic and western Mediterranean source areas for precipitation to Corchia Cave[68] is consistent with addition of ~0.3 Sverdrup (Sv, 10^{-6} m^3 s^{-1}; Fig. 4a) of isotopically light (assumed −40‰) meltwater to a 80-m-deep mixed layer with $\delta^{18}O$ of 1‰ (ref. 69). This implies a mixing ratio between marine and meltwater end-members of 40:1 and scales the marine flux in the Subtropical Atlantic to approximately 12 Sv. Despite the roughness of our calculation this overall agrees with a complete collapse of the thermohaline component of the Gulf Stream in the Subtropical North Atlantic during HS11 and with the persistence of only the wind-driven marine transport, which today accounts for ~17 Sv (ref. 70).

32. Comas, M. C., Zahn, R. & Klaus, A. Mediterranean Sea II: The Western Mediterranean. *Proc. ODP Init. Rep.* **161,** http://dx.doi.org/10.2973/odp.proc.ir.161.1996 (1996).
33. Pinardi, N. & Masetti, E. Variability of the large scale general circulation of the Mediterranean Sea from observations and modelling: a review. *Palaeogeogr. Palaeoclimatol. Palaeoecol.* **158,** 153–173 (2000).
34. Pinardi, N. *et al.* Mediterranean Sea large-scale low-frequency ocean variability and water mass formation rates from 1987 to 2007: a retrospective analysis. *Prog. Oceanogr.* **132,** 318–332 (2015).
35. Malanotte-Rizzoli, P. *et al.* Physical forcing and physical/biochemical variability of the Mediterranean Sea: a review of unresolved issues and directions for future research. *Ocean Sci.* **10,** 281–322 (2014).
36. Rohling, E. J., Marino, G. & Grant, K. M. Mediterranean climate and oceanography, and the periodic development of anoxic events (sapropels). *Earth Sci. Rev.* **143,** 62–97 (2015).
37. Marino, G. *et al.* Aegean Sea as driver of hydrographic and ecological changes in the eastern Mediterranean. *Geology* **35,** 675–678 (2007).
38. Rohling, E. J. *et al.* Reconstructing past planktic foraminiferal habitats using stable isotope data: a case history for Mediterranean sapropel S5. *Mar. Micropaleontol.* **50,** 89–123 (2004).
39. Friedrich, O. *et al.* Influence of test size, water depth, and ecology on Mg/Ca, Sr/Ca, $\delta^{18}O$ and delta $\delta^{13}C$ in nine modern species of planktic foraminifers. *Earth Planet. Sci. Lett.* **319–320,** 133–145 (2012).
40. Incarbona, A., Sprovieri, M., Lirer, F. & Sprovieri, R. Surface and deep water conditions in the Sicily channel (central Mediterranean) at the time of sapropel S5 deposition. *Palaeogeogr. Palaeoclimatol. Palaeoecol.* **306,** 243–248 (2011).
41. Myers, P. G., Haines, K. & Rohling, E. J. Modeling the paleocirculation of the Mediterranean: the last glacial maximum and the Holocene with emphasis on the formation of sapropel S1. *Paleoceanography* **13,** 586–606 (1998).
42. Rogerson, M. *et al.* Enhanced Mediterranean-Atlantic exchange during Atlantic freshening phases. *Geochem. Geophys. Geosyst.* **11,** Q08013 (2010).
43. Rohling, E. J. *et al.* Abrupt cold spells in the northwest Mediterranean. *Paleoceanography* **13,** 316–322 (1998).
44. Rohling, E. J. *et al.* African monsoon variability during the previous interglacial maximum. *Earth Planet. Sci. Lett.* **202,** 61–75 (2002).
45. Rohling, E. J., Hopmans, E. C. & Damste, J. S. S. Water column dynamics during the last interglacial anoxic event in the Mediterranean (sapropel S5). *Paleoceanography* **21,** PA2018 (2006).
46. van der Meer, M. T. J. *et al.* Hydrogen isotopic compositions of long-chain alkenones record freshwater flooding of the Eastern Mediterranean at the onset of sapropel deposition. *Earth Planet. Sci. Lett.* **262,** 594–600 (2007).
47. Casford, J. S. L. *et al.* A dynamic concept for eastern Mediterranean circulation and oxygenation during sapropel formation. *Palaeogeogr. Palaeoclimatol. Palaeoecol.* **190,** 103–119 (2003).
48. Osborne, A. H., Marino, G., Vance, D. & Rohling, E. J. Eastern Mediterranean surface water Nd during Eemian sapropel S5: monitoring northerly (mid-latitude) versus

southerly (sub-tropical) freshwater contributions. *Quat. Sci. Rev.* **29,** 2473–2483 (2010).
49. Grelaud, M., Marino, G., Ziveri, P. & Rohling, E. J. Abrupt shoaling of the nutricline in response to massive freshwater flooding at the onset of the last interglacial sapropel event. *Paleoceanography* **27,** PA3208 (2012).
50. Piccini, L. *et al.* The environmental features of the Monte Corchia cave system (Apuan Alps, central Italy) and their effects on speleothem growth. *Int. J. Speleol.* **37,** 153–172 (2008).
51. Bard, E. *et al.* Hydrological conditions over the western Mediterranean basin during the deposition of the cold Sapropel 6 (ca. 175 kyr BP). *Earth Planet. Sci. Lett.* **202,** 481–494 (2002).
52. Marino, G. *et al.* Early and middle Holocene in the Aegean Sea: interplay between high and low latitude climate variability. *Quat. Sci. Rev.* **28,** 3246–3262 (2009).
53. Badertscher, S. *et al.* Pleistocene water intrusions from the Mediterranean and Caspian seas into the Black Sea. *Nature Geosci.* **4,** 236–239 (2011).
54. Regattieri, E. *et al.* A continuous stable isotope record from the penultimate glacial maximum to the Last Interglacial (159-121 ka) from Tana Che Urla Cave (Apuan Alps, central Italy). *Quat. Res.* **82,** 450–461 (2014).
55. Veres, D. *et al.* The Antarctic ice core chronology (AICC2012): an optimized multi-parameter and multi-site dating approach for the last 120 thousand years. *Clim. Past.* **9,** 1733–1748 (2013).
56. Landais, A. *et al.* Two-phase change in CO_2, Antarctic temperature and global climate during Termination II. *Nature Geosci.* **6,** 1062–1065 (2013).
57. Schneider, R., Schmitt, J., Koehler, P., Joos, F. & Fischer, H. A reconstruction of atmospheric carbon dioxide and its stable carbon isotopic composition from the penultimate glacial maximum to the last glacial inception. *Clim. Past.* **9,** 2507–2523 (2013).
58. Martrat, B. *et al.* Abrupt temperature changes in the Western Mediterranean over the past 250,000 years. *Science* **306,** 1762–1765 (2004).
59. Martrat, B. *et al.* Four climate cycles of recurring deep and surface water destabilizations on the Iberian margin. *Science* **317,** 502–507 (2007).
60. Rohling, E. J. *et al.* Sea-level and deep-sea-temperature variability over the past 5.3 million years. *Nature* **508,** 477–482 (2014).
61. Rohling, E. J. & Bryden, H. L. Estimating past changes in the eastern Mediterranean fresh-water budget, using reconstructions of sea-level and hydrography. *Proc. Kon. Ned. Akad. B* **97,** 201–217 (1994).
62. Rohling, E. J. Environmental control on Mediterranean salinity and $\delta^{18}O$. *Paleoceanography* **14,** 706–715 (1999).
63. Schrag, D. P. *et al.* The oxygen isotopic composition of seawater during the Last Glacial Maximum. *Quat. Sci. Rev.* **21,** 331–342 (2002).
64. Mikolajewicz, U. Modeling Mediterranean Ocean climate of the Last Glacial Maximum. *Clim. Past.* **7,** 161–180 (2011).
65. Kim, S. T. & O'Neil, J. R. Equilibrium and nonequilibrium oxygen isotope effects in synthetic carbonates. *Geochim. Cosmochim. Acta* **61,** 3461–3475 (1997).
66. Lachniet, M. S. Climatic and environmental controls on speleothem oxygen-isotope values. *Quat. Sci. Rev.* **28,** 412–432 (2009).
67. Dansgaard, W. Stable isotopes in precipitation. *Tellus* **16,** 436–468 (1964).
68. Drysdale, R. N. *et al.* Palaeoclimatic implications of the growth history and stable isotope ($\delta^{18}O$ and $\delta^{13}C$) geochemistry of a Middle to Late Pleistocene stalagmite from central-western Italy. *Earth Planet. Sci. Lett.* **227,** 215–229 (2004).
69. LeGrande, A. N. & Schmidt, G. A. Global gridded data set of the oxygen isotopic composition in seawater. *Geophys. Res. Lett.* **33,** L12604 (2006).
70. Lynch-Stieglitz, J., Curry, W. B. & Slowey, N. Weaker Gulf Stream in the Florida straits during the last glacial maximum. *Nature* **402,** 644–648 (1999).
71. Berger, A. L. Long-term variations of daily insolation and Quaternary climatic changes. *J. Atmos. Sci.* **35,** 2362–2367 (1978).
72. Berger, A. L. Long-term variations of caloric insolation resulting from Earth's orbital elements. *Quat. Res.* **9,** 139–167 (1978).
73. Berger, A. & Loutre, M. F. Long-term variations in insolation and their effects on climate, the LLN experiments. *Surv. Geophys.* **18,** 147–161 (1997).
74. Monnin, E. *et al.* Atmospheric CO_2 concentrations over the last glacial termination. *Science* **291,** 112–114 (2001).
75. Schmitt, J. *et al.* Carbon isotope constraints on the deglacial CO_2 rise from ice cores. *Science* **336,** 711–714 (2012).
76. Ahn, J. & Brook, E. J. Siple Dome ice reveals two modes of millennial CO_2 change during the last ice age. *Nature Commun.* **5,** 3723 (2014).
77. Andersen, K. K. *et al.* High-resolution record of Northern Hemisphere climate extending into the last interglacial period. *Nature* **431,** 147–151 (2004).
78. Stenni, B. *et al.* The deuterium excess records of EPICA Dome C and Dronning Maud Land ice cores (East Antarctica). *Quat. Sci. Rev.* **29,** 146–159 (2010).
79. Clark, P. U. *et al.* The Last Glacial Maximum. *Science* **325,** 710–714 (2009).

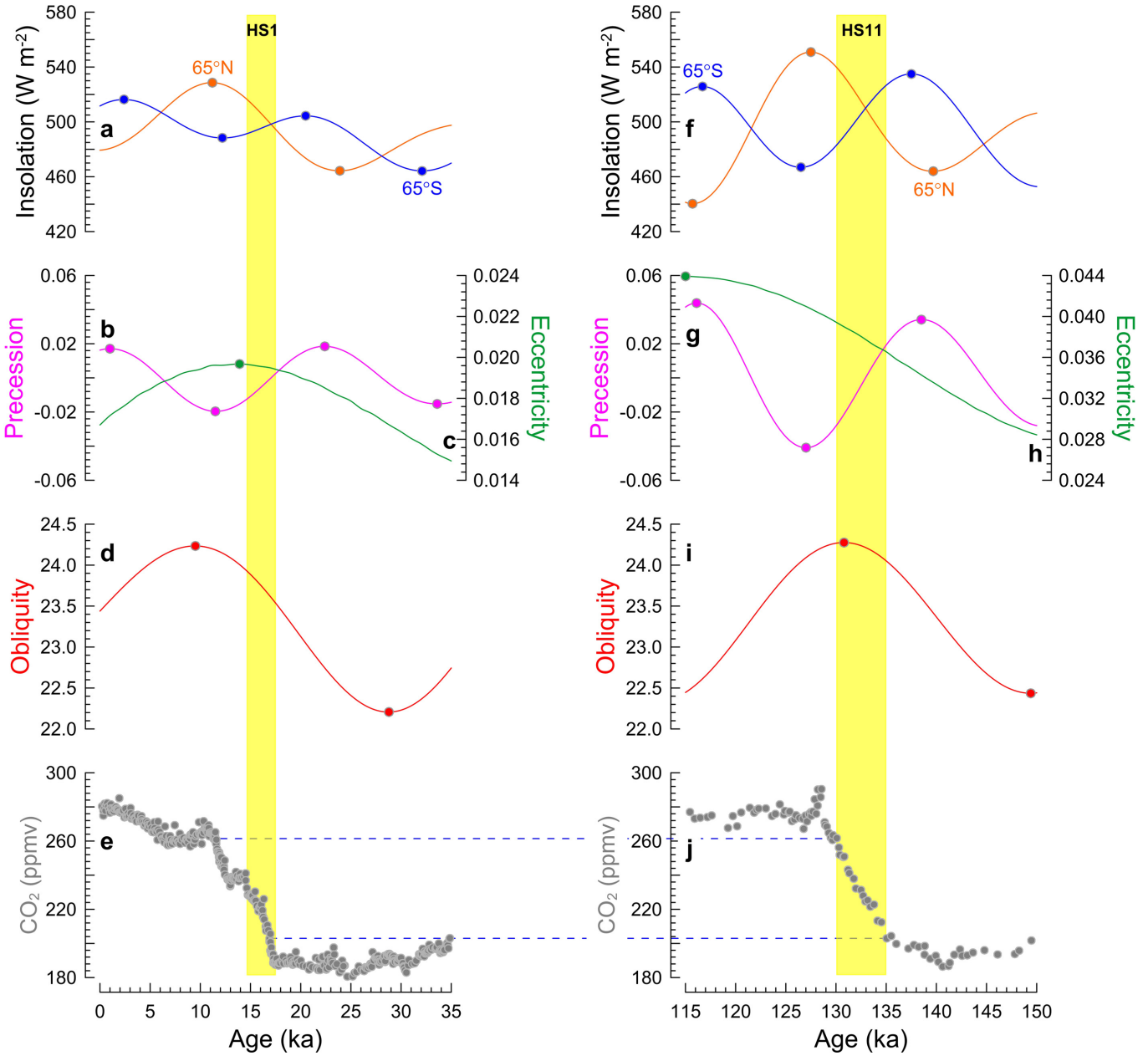

Extended Data Figure 1 | Orbital parameters, insolation forcing, and atmospheric CO_2 concentrations during the last two glacial–interglacial transitions. **a**, **f**, Incoming solar radiation on 21 June and 21 December at 65° N (orange) and 65° S (blue), for T-I (**a**) and T-II (**f**)[31]. **b**, **g**, Precession of the Earth's axis[31] for T-I (**b**) and T-II (**g**). **c**, **h**, as **b**, **g**, but for eccentricity of the Earth's orbit[31]. Note the different axis scales in **c** and **h**. **d**, **i**, Obliquity of the Earth's axis[31] for T-I (**d**) and T-II (**i**). Different orbital configurations during glacial terminations I (T-I) and II (T-II) led to markedly different insolation forcing[31,71–73], with the summer 65° N insolation increase during T-II larger by ~35% (~23 W m^{-2}), and occurring at faster rates[18], than that during T-I. **e**, **j**, atmospheric CO_2 concentrations during T-I (refs 74–76) and T-II (ref. 56). Yellow bands illustrate the timing of Heinrich stadial 1 (HS1) and 11 (HS11), following previous literature[1] and this study, respectively. Dashed blue lines highlight that atmospheric CO_2 concentrations were systematically higher during T-II than during T-I. Symbols indicate the maxima and/or minima in insolation, precession, eccentricity, and obliquity cycles.

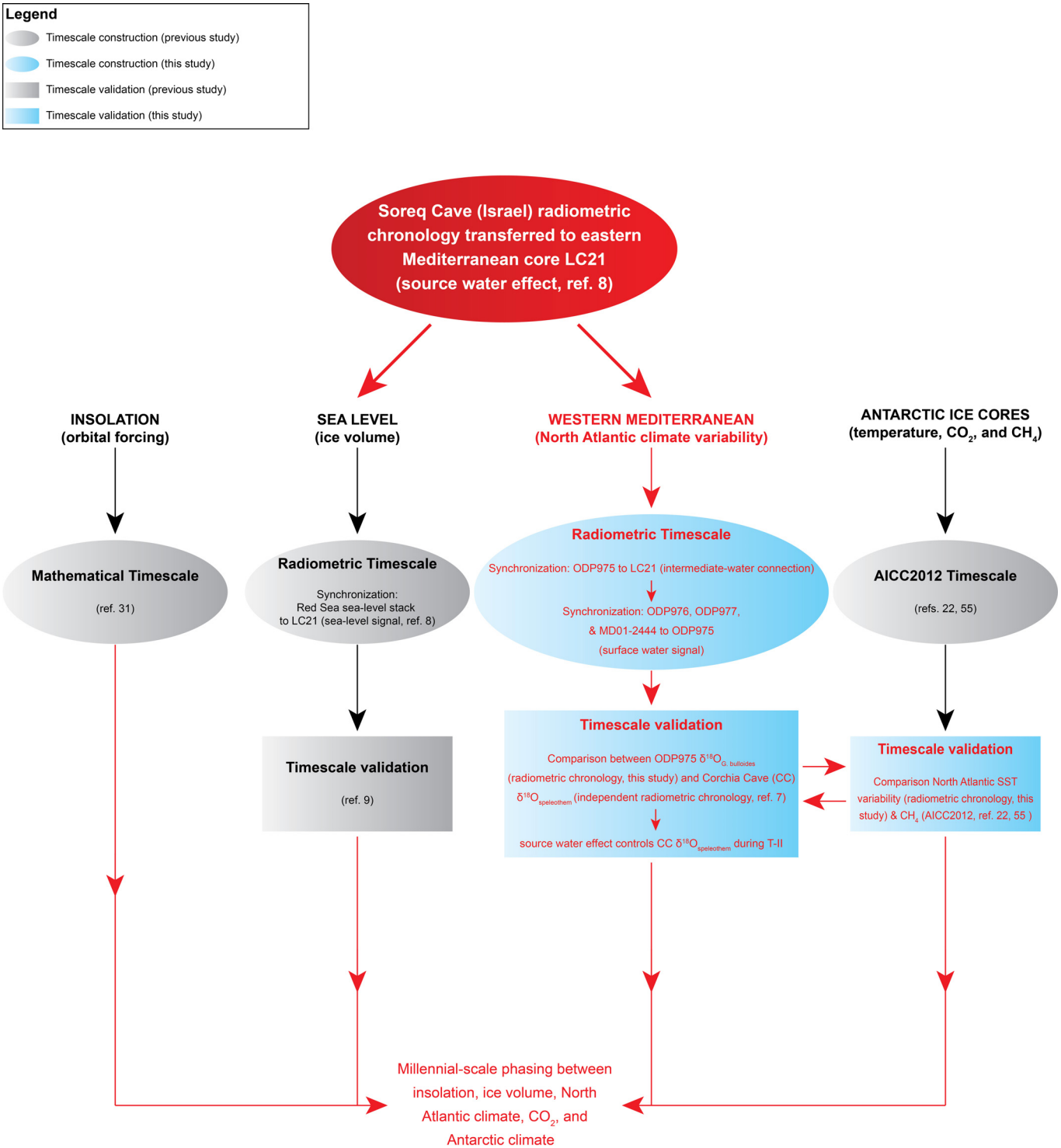

Extended Data Figure 2 | Flowchart of the approach used to construct and validate chronologies of the various records. See main text and Methods for details.

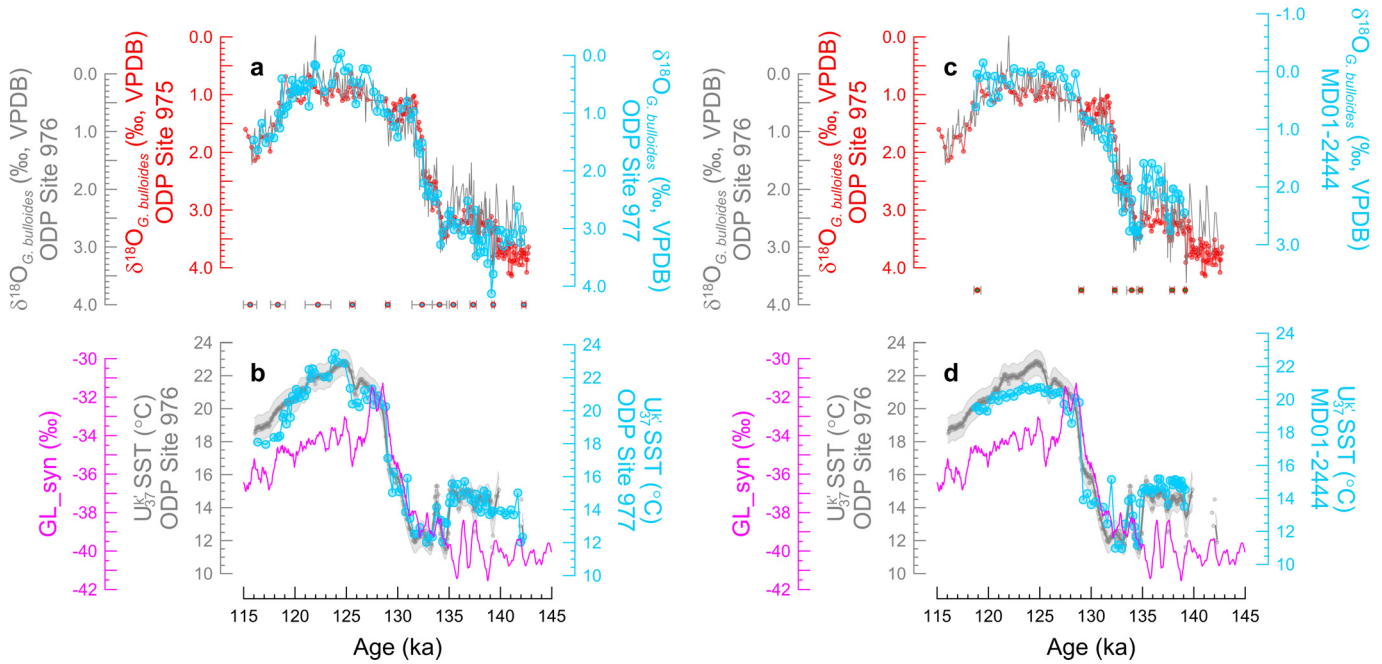

Extended Data Figure 3 | Synchronization of western Mediterranean Sea ODP975 to ODP977 and Iberian Margin core MD01-2444. **a**, Synchronization of *G. bulloides* $\delta^{18}O$ from western Mediterranean ODP977 to its counterpart from nearby ODP975. Circles and error bars depict tie points and 2σ synchronization errors, respectively (Methods, Extended Data Table 3). The *G. bulloides* $\delta^{18}O$ from ODP976 is only shown for comparison and is not used to transfer our new, radiometrically constrained chronology, to ODP977 (Methods). **b**, Validation of the synchronization exercise shown in **a** by comparing the alkenone-based sea surface temperature (SST) records from ODP977 and ODP976, on their new, radiometrically constrained chronology. The 95% confidence intervals (light grey envelope) and probability maximum (heavier grey line) and its associated 95% confidence intervals (heavier grey envelope) of the ODP976 SST data (grey circles) are based on a Monte Carlo analysis of chronological and SST uncertainties, employing a 0.2 kyr Gaussian filter (Methods). The synthetic record of Greenland climate variability[16] is also shown. **c**, Synchronization of the *G. bulloides* $\delta^{18}O$ from Iberian Margin (Atlantic Ocean) core MD01-2444 to its counterpart from ODP975 (Western Mediterranean, Methods). Circles and error bars depict tie points and 2σ synchronization errors, respectively (Methods, Extended Data Table 3). The *G. bulloides* $\delta^{18}O$ from ODP976 is shown for comparison and is not used to transfer the MD01-2444 records to our new, radiometrically constrained chronology (Methods). **d**, Validation of the synchronization exercise shown in **c** by comparing alkenone-based SST records from core MD01-2444 and ODP976 (shaded envelopes and circles as in **b**), on their new radiometrically constrained chronology. The synthetic record of Greenland climate variability[16] is also shown.

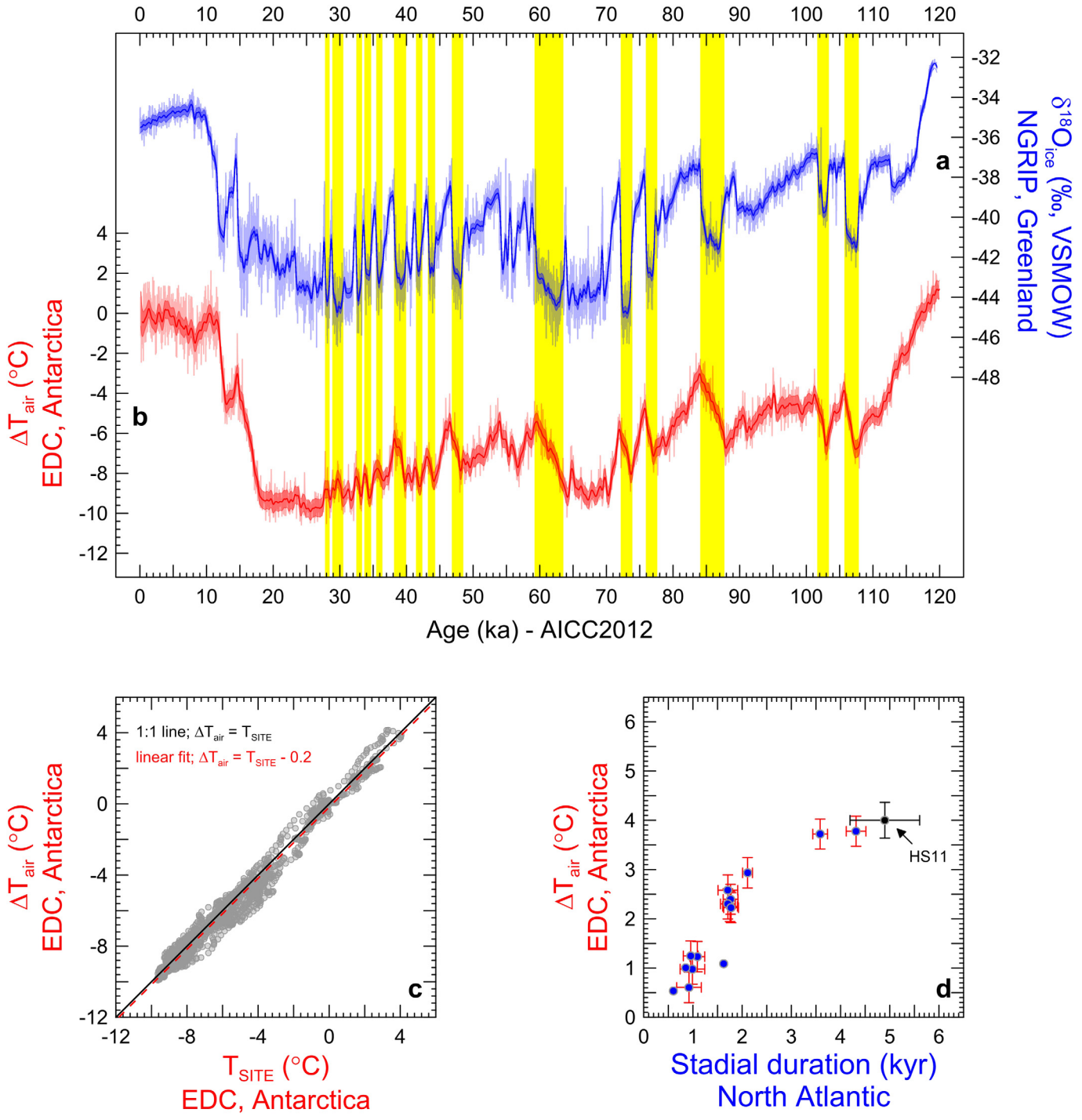

Extended Data Figure 4 | Relationship between the duration of the North Atlantic cold phases (stadials) and the magnitude of Antarctic warming. **a**, $\delta^{18}O_{ice}$ time series from North Greenland Ice Core Project (NGRIP)[77] (light blue). The probability maximum (solid blue line) and associated 95% confidence bounds (shaded blue envelope) of the $\delta^{18}O_{ice}$ record result from 10,000 Monte Carlo simulations, employing a 0.15 kyr Gaussian filter through the data and their chronological and $\delta^{18}O_{ice}$ uncertainties (see Methods). **b**, EPICA Dome C (EDC) temperature reconstructions (ΔT) based on δD_{ice} data[13] (light red). The probability maximum (solid red line) and associated 95% confidence bounds (shaded red envelope) of the temperature record result from 10,000 Monte Carlo simulations, employing a 0.2 kyr Gaussian filter through the data and their chronological and ΔT uncertainties. **c**, Comparison between Antarctic temperature reconstructions from EDC using the methods of Jouzel *et al.* (ΔT, ref. 13) and Stenni *et al.* (T_{SITE}, ref. 78), revealing no difference in the amplitude of the estimated Antarctic temperature shifts. **d**, Relationship between duration of Greenland stadials and Antarctic warming for bipolar seesaw events highlighted in **a** and **b** by yellow bands. Greenland and Antarctic records are on the latest ice core chronology AICC2012 (ref. 55). Error bars depict 1σ uncertainty in the magnitude and duration of North Atlantic cooling.

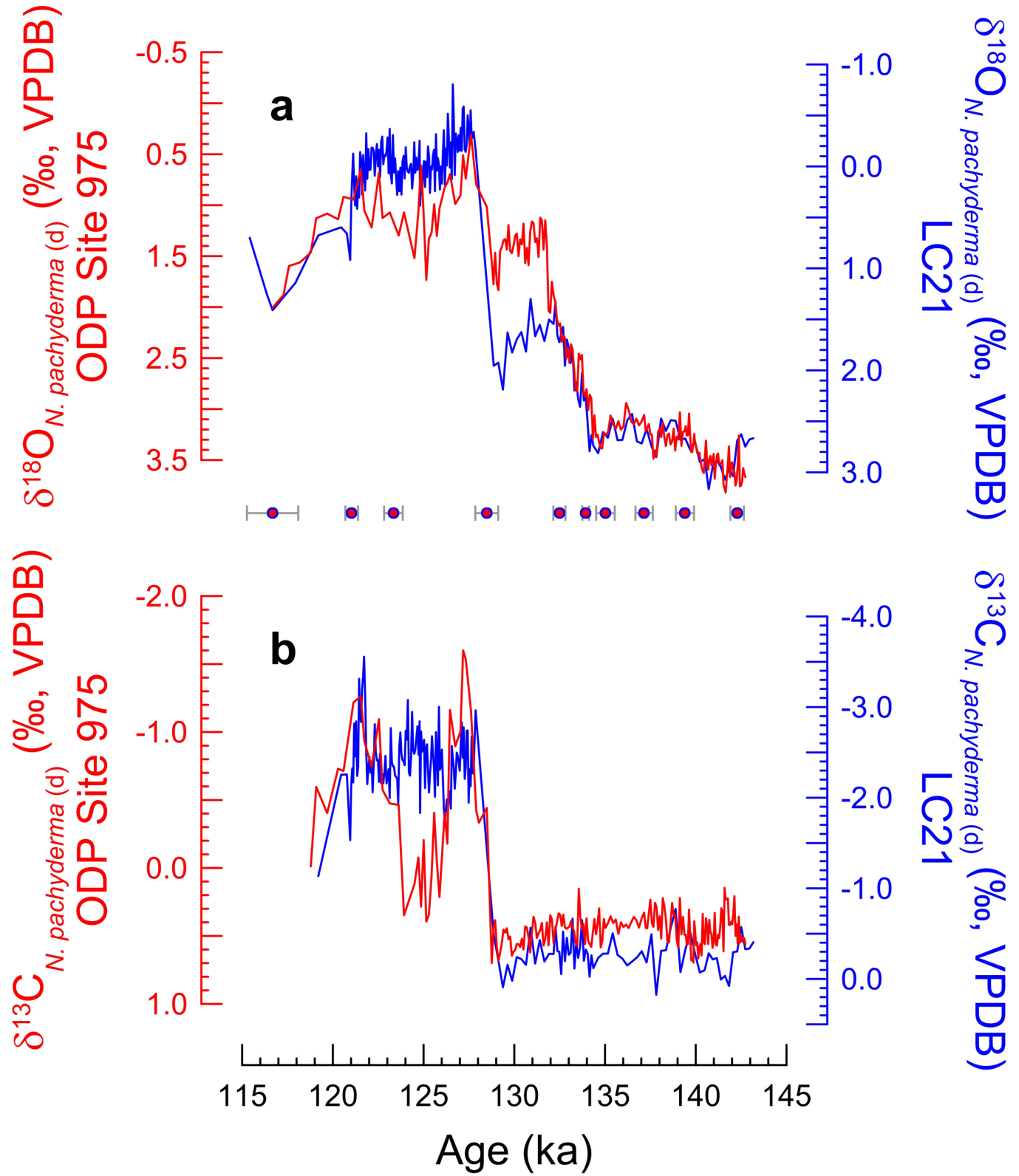

Extended Data Figure 5 | Synchronization of western Mediterranean Sea ODP975 to eastern Mediterranean core LC21. **a**, Synchronization of the *N. pachyderma* (d) $\delta^{18}O$ from ODP975 to its counterpart from eastern Mediterranean core LC21 (Methods), which was placed on a radiometric chronology by ref. 8. Red filled circles and error bars depict the tie points used to synchronize ODP975 to LC21 and the 2σ synchronization uncertainties, respectively. **b**, Validation of the synchronization exercise shown in **a** by comparing the respective co-registered *N. pachyderma* (d) $\delta^{13}C$ profiles from the same cores.

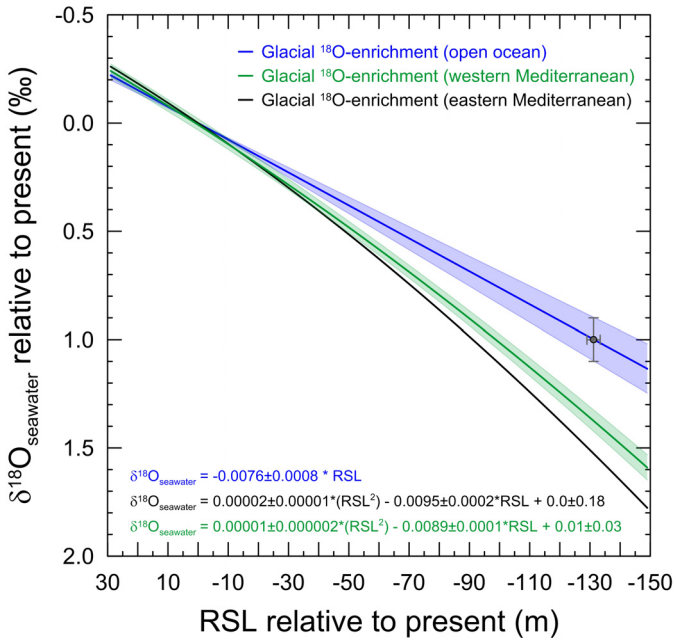

Extended Data Figure 6 | Glacial ^{18}O-enrichment in oceanic and Mediterranean seawater. Blue (open ocean), black (eastern Mediterranean Sea) and green (western Mediterranean Sea) lines illustrate the relationship between seawater $\delta^{18}O$ ($\delta^{18}O_{seawater}$) and relative sea level (RSL). The open ocean relationship has been re-calculated here using the latest assessment (grey symbol) of the sea-level lowstand[11] of the Last Glacial Maximum (26.5–19 ka, ref. 79) and the mean ocean $\delta^{18}O_{seawater}$ value derived from porewater analyses in a suite of deep-sea cores[63]. The eastern Mediterranean relationship is derived from the model presented in ref. 60. The western Mediterranean relationship (green line) reflects linear mixing between eastern Mediterranean (black line) and open ocean (blue line) end-members, assuming that the residence time effect[60,62] on $\delta^{18}O_{seawater}$ (and salinity) in the western Mediterranean is 70 ± 5% of that in eastern Mediterranean[64]. Shaded envelopes are 1σ confidence bounds, derived from probabilistic analysis of uncertainties.

Extended Data Table 1 | Synchronization of ODP975 to LC21

Age (ka BP)	ODP975 sample spacing (kyr)	LC21 sample spacing (kyr)	MSE synchronization (kyr)	MSE age uncertainty (kyr)
116.68	0.50	0.50	0.71	1.52
121.04	0.04	0.04	0.17	1.76
123.34	0.07	0.05	0.26	1.56
128.48	0.22	0.22	0.31	1.20
132.49	0.12	0.12	0.17	1.17
133.94	0.04	0.08	0.09	0.59
135.02	0.16	0.20	0.26	0.56
137.16	0.09	0.22	0.24	0.93
139.40	0.08	0.24	0.25	1.33
142.28	0.11	0.15	0.19	1.50

Sample spacing (1σ) uncertainties in ODP975 and LC21 and dating (1σ) uncertainties of LC21 (ref. 7) are combined in mean squared estimates (MSE). Tie-points in red include extra uncertainty (3 times the sample spacing).

Extended Data Table 2 | Synchronization of ODP976 to ODP975

Age (ka BP)	ODP976 sample spacing (kyr)	ODP975 sample spacing (kyr)	MSE synchronization	MSE age uncertainty (kyr)
115.63	0.18	0.23	0.29	1.54
118.33	0.03	0.25	0.25	1.59
122.24	0.26	0.18	0.31	1.76
125.02	0.21	0.36	0.41	1.52
129.04	0.06	0.08	0.10	1.20
132.45	0.07	0.08	0.11	1.18
133.98	0.14	0.08	0.16	0.76
135.08	0.07	0.09	0.11	0.58
137.34	0.08	0.08	0.12	0.92
137.97	0.02	0.06	0.07	1.06
139.36	0.06	0.06	0.08	1.30
142.28	0.54	0.16	0.56	1.57

Sample spacing (1σ) uncertainties in ODP976 and ODP975 and dating uncertainties of ODP975 (see Extended Data Table 1) are combined in mean squared estimates (MSE). Tie-points in red include extra uncertainty (3 times the sample spacing).

Extended Data Table 3 | Synchronization of ODP977 to ODP975

Age (ka BP)	ODP977 sample spacing (kyr)	ODP975 sample spacing (kyr)	MSE synchronization	MSE age uncertainty (kyr)
115.63	0.23	0.23	0.32	1.55
118.33	0.25	0.25	0.35	1.65
122.24	0.60	0.18	0.63	1.77
125.59	0.10	0.10	0.14	1.41
129.04	0.08	0.08	0.11	1.20
132.38	0.49	0.08	0.50	1.20
134.07	0.34	0.08	0.35	0.72
135.41	0.16	0.12	0.20	0.67
137.34	0.13	0.08	0.16	0.98
139.30	0.03	0.06	0.06	1.31
142.28	0.09	0.05	0.10	1.47

Sample spacing (1σ) uncertainties in ODP977 and ODP975 and dating uncertainties of ODP975 (see Extended Data Table 1) are combined in mean squared estimates (MSE).

Extended Data Table 4 | Synchronization of core MD01-2444 to ODP975.

Age (ka BP)	MD01-2444 sample spacing (kyr)	ODP975 sample spacing (kyr)	MSE synchronization	MSE age uncertainty (kyr)
118.930	0.075	0.150	0.168	1.640
129.035	0.079	0.092	0.121	1.203
132.300	0.077	0.077	0.108	1.177
133.955	0.227	0.101	0.249	0.718
134.810	0.065	0.065	0.092	0.576
137.885	0.108	0.043	0.116	1.031
139.165	0.015	0.045	0.047	1.281

Sample spacing (1σ) uncertainties in MD01-2444 and ODP975 and dating uncertainties of ODP975 (see Extended Data Table 1) are combined in mean squared estimates (MSE).